

Investigation of Electrolyte Decomposition Byproducts in Gas and Liquid Phases Due to Water Impurities in Large-Scale Acetonitrile-Based Supercapacitors

Jiraporn Phojaroen,^[a] Phatsawit Wuamprakhon,^[a] Thitiphum Sangsanit,^[a] Kanruthai Santiyuk,^[a] Kan Homlamai,^[a] Nichakarn Anansuksawat,^[a] Worapol Tejangkura,^[a] Ronnachai Songthan,^[a] and Montree Sawangphruk^{*[a]}

This study investigates the impact of water impurities on electrolyte decomposition in large-scale cylindrical supercapacitors, with a focus on acetonitrile-based electrolytes. The research identified ethylene, ethane, and nitrogen as primary gaseous byproducts and acetamide, N-ethyl acetamide, and trimethylsilyl acetamide as major liquid-phase decomposition products. Advanced analytical techniques, including in-situ gas chromatography and nuclear magnetic resonance, revealed that water impurities significantly accelerate electrolyte degradation. The findings demonstrate that water-induced decomposition mechanisms involve intricate pathways, including

Hofmann elimination and hydrolysis reactions. Additionally, the presence of water catalyzes the formation of new byproducts, impacting both the electrolyte and electrode stability. This comprehensive analysis provides critical insights into the degradation processes of supercapacitors, emphasizing the need for stringent control of water content to enhance device longevity and performance. The study's outcomes suggest potential strategies for optimizing electrolyte compositions and electrode materials to mitigate degradation and improve supercapacitor efficiency.

Introduction

Supercapacitors, electrochemical energy storage devices distinguished by their remarkable power density (ca. 1–2 kW/kg),^[1] reasonable energy density (1.5–5.0 Wh/kg),^[1,2] extended cycle life (100,000–1,000,000 cycles), and rapid charge/discharge capabilities, have garnered substantial interest for a myriad of applications, including regenerative braking in electric vehicles,^[3] power backup systems, consumer electronics, public transportation, medical devices, and telecommunications.^[1,4] Despite their attractive attributes, the longevity and performance of supercapacitors are inherently compromised by the inevitable decomposition of electrolytes, a process that culminates in the obstruction of electrode pores through the accumulation of decomposition byproducts and gas evolution, consequently triggering capacity fading and an upsurge in internal resistance.

At the root of this challenge lies the decomposition of acetonitrile (ACN)-based electrolytes,^[5] which constitute the state-of-the-art electrolyte in commercial supercapacitors. This degradation transpires through a multitude of intricate mechanisms, including hydrolysis, polymerization, Hofmann elimina-

tion, and fluorination.^[5b] The presence of trace amounts of water impurities within the ACN solvent serves as the catalyst for these deleterious reactions, initiating the hydrolysis of ACN and leading to many uncertain byproducts,^[5a,b] which are not yet fully understood due to unclear reaction mechanisms. Besides, prior studies have predominantly focused on the ramifications of water in diminutive setups like coin cells, which do not represent the large-scale supercapacitors using thick electrodes having different electrode crosstalks with thin electrode. As a result, our research ventured into the exploration of water's impact on electrolyte and electrode decomposition, alongside gas evolution, within a large-scale system, bridging a critical gap in the existing literature. Specifically, we examined a jellyroll closed system equipped with thin activated carbon electrodes in 18650 cylindrical cell double-layer capacitors (EDLCs), operating at peak voltage, thereby simulating real-world conditions including thick electrode crosstalk leading to discoveries of new byproducts and their contents, which are different from previous reports. Notably, the cylindrical cell here, which is similar to the battery technology,^[6] has not been widely investigated in the supercapacitor's community.^[7]

Through the application of in-situ gas chromatography, a powerful analytical technique, we identified and quantified the gaseous decomposition products evolved during the degradation process. Moreover, the extent of acetamide generation, a key indicator of electrolyte decomposition, is meticulously quantified employing gas chromatography-mass spectrometry (GC-MS) and nuclear magnetic resonance (NMR), providing invaluable insights into the kinetics and mechanisms of this deleterious process.^[5b] To gain a comprehensive understanding of the degradation processes at play, a multi-faceted analytical

[a] J. Phojaroen, P. Wuamprakhon, T. Sangsanit, K. Santiyuk, K. Homlamai, N. Anansuksawat, W. Tejangkura, R. Songthan, M. Sawangphruk
Center of Excellence for Energy Storage Technology (CEST), School of Energy Science and Engineering (ESE), Vidyasirimedhi Institute of Science and Technology (VISTEC), 555 Moo 1 Payupnai, Wangchan District, Rayong 21210, Thailand
E-mail: montree.s@vistec.ac.th

 Supporting information for this article is available on the WWW under
<https://doi.org/10.1002/batt.202400738>

approach is employed. The aftermath analysis of the electrode and salt was conducted using a suite of many characterization techniques, including Wavelength Dispersive X-ray fluorescence (WDXRF), Scanning Electron Microscopy and Energy-Dispersive X-ray Spectroscopy (SEM-EDX), Fourier-transform infrared spectroscopy (FTIR), and X-Ray photoelectron spectroscopy (XPS). These techniques enable the elucidation of the changes in elemental composition, morphology, functional groups, and surface chemistry of the electrodes, painting a holistic picture of the intricate degradation mechanisms.

The findings of degradation mechanisms at thick electrodes and large-scale supercapacitors hold profound implications for the design and development of more durable and efficient supercapacitors. By elucidating the intricate interplay between water impurities, electrolyte decomposition, and electrode degradation, we pave the way for the formulation of strategies to mitigate these detrimental processes. Potential avenues include the optimization of electrode materials, the development of novel electrolyte compositions with enhanced stability and lower water susceptibility, and the implementation of stringent purification protocols to minimize water contamination. Ultimately, this research underscores the pivotal role of water in dictating the longevity and performance of supercapacitors, a critical consideration in the quest to harness the full potential of these promising energy storage devices for a wide array of applications in the modern era.

Experimental Section

Materials and Chemical Reagents

This research utilized a range of materials, including supercapacitor-graded activated carbon (AC, YP80F, supplied by GELON), carbon black (Super P, provided by TIMCAL), sodium carboxymethylcellulose (NaCMC, from Sigma-Aldrich), styrene-butadiene rubber (SBR, obtained from Sigma-Aldrich), 18 µm aluminum foil (sourced from GELON LIB), Al₂O₃ ceramic coated tri-layer polypropylene-polyethylene-polypropylene (PP-PE-PP) separators (acquired from GELON LIB), tetraethylammonium tetrafluoroborate salt (TEABF₄, courtesy of GELON LIB), acetonitrile solvent (ACN, from Sigma-Aldrich), dimethyl sulfoxide-d6 (DMSO-d6, Sigma-Aldrich), 1,4-dinitrobenzene used as an internal standard, (Sigma-Aldrich), methanol (MeOH, EMSURE® ACS grade), and deionized water from a Milli-Q system (DI water, with a resistivity of 15 MΩ cm, sourced from Millipore).

Fabrication of Large-Scale Electrodes at a Pilot Plant Scale

The electrode fabrication process was carried out in a pilot-scale manufacturing facility equipped with a dry room (dew point of -50°C), with the electrode composition meticulously formulated to comprise 95.2% activated carbon (AC), 2.4% carbon black (CB), 1.2% carboxymethylcellulose (CMC), and 1.2% styrene-butadiene rubber (SBR). This carefully engineered mixture was blended with deionized (DI) water until achieving a homogeneous slurry with a honey-like texture and a viscosity of approximately 9140 mPas, as determined by rheological characterization. Subsequent to the preparation of the electrode slurry, it was cast onto aluminum foil using a precise coating technique, ensuring uniform distribution and thickness. The coated foil was then subjected to a controlled

drying process in a convection oven, maintained at an elevated temperature overnight to facilitate the evaporation of residual solvent and the formation of a robust electrode film. The dried AC electrode was then subjected to a compression process under a substantial pressure of 2 tons, resulting in a dense and compact structure with a meticulously controlled thickness of 200 µm, as verified by high-resolution field-emission scanning electron microscopy (FE-SEM) analysis, depicted in Figure 1B. The electrode, with dimensions of 15 cm \times 46 cm, was subsequently precision-cut and wound with a separator membrane to assemble a robust 18650 cylindrical cell configuration. To ensure the quality and integrity of the electrode components, a comprehensive characterization protocol was implemented. The physical morphology and microstructural features of the electrode were meticulously examined using FE-SEM, as illustrated in Figure 1A, providing valuable insights into the distribution and integration of the constituent materials within the electrode matrix. Furthermore, thermogravimetric analysis (TGA) was employed to elucidate the thermal stability and decomposition behavior of the electrode components, as depicted in Figure 1C. This analytical technique facilitated the identification of potential thermal degradation pathways and the determination of the temperature range over which the electrode materials exhibit structural and chemical stability, critical considerations for the reliable operation of the supercapacitor system. The meticulous attention to detail in the electrode fabrication process, coupled with the rigorous characterization protocols, ensured the production of high-quality electrodes tailored for the demanding requirements of large-scale supercapacitor applications, laying the foundation for the subsequent investigation of water-induced degradation mechanisms.

Electrolyte Preparation

The advanced electrolyte formulation employed for the EDLCs in this study consisted of a 1 M TEABF₄ solution in ACN. The preparation of this electrolyte involved the precise weighing and dissolution of 54.265 g of the TEABF₄ salt in ACN solvent, followed by volumetric adjustment to a final volume of 250 ml using a calibrated volumetric flask, ensuring accurate concentration and minimizing potential variability. A series of electrolyte solutions

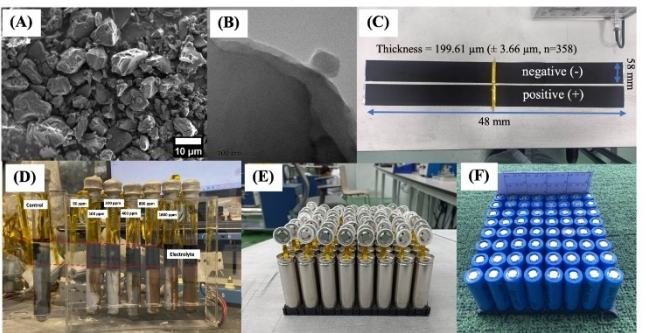


Figure 1. Microscopic and Assembly Visualizations of AC Electrodes in 18650 Cylindrical Cells; Panel (A) displays a Field Emission Scanning Electron Microscopy (FE-SEM) top view of the AC electrode powder, highlighting the surface morphology. Panel (B) presents a High-Resolution Transmission Electron Microscopy (HRTEM) image of AC, showcasing the detailed structural features. Panel (C) illustrates both negative and positive electrodes, demonstrating their comparative physical characteristics. Panel (D) depicts the jelly roll configuration incorporating the 18650 AC electrode, revealing the intricate winding process. Panel (E) captures the moment of electrolyte injection into 18650 cylindrical cells, detailing the procedure of cell assembly. Panel (F) shows the wrapped 18650 cylindrical cells post-assembly, ready for testing or application.

with carefully controlled water concentrations were prepared to investigate the effects of varying water contents on the electrochemical performance and degradation mechanisms of the EDLCs. The inherent water content in the ACN solvent was systematically adjusted, and the water content in the 1.0 M TEABF₄ in ACN solution was measured using NMR, with 1,4-dinitrobenzene as the internal standard, as outlined in Table S1 and Figure S1 of the Supplementary Information. Each modified solvent was subsequently employed to formulate the corresponding electrolyte solution within an inert atmosphere glovebox, maintaining an argon environment to minimize potential contamination and ensure the preservation of the electrolyte's purity and integrity. This meticulous approach to electrolyte preparation, coupled with the stringent control of water content and the implementation of inert atmospheric conditions, ensured the reproducibility and reliability of the experimental procedures, enabling a comprehensive investigation of the intricate interplay between water impurities and the degradation processes within the EDLC system.

A Jelly-Roll Setup and Testing Protocol

Using the glass tube with 180 mm height and 20 mm ID and 18650 cylindrical cells of supercapacitor from the CEST pilot plant, added 20 ml of electrolyte (Figures 1D and S2) The first step checks the performance of each cell by galvanostatic charge-discharge (GCD) test at difference currents 100, 250, 500, 750, 1000, 2500, and 100 mA with constant voltage at 4.1 V after that, using abused voltage with the regular current charge at 100 mA from open circuit voltage (OCV) until 4.1 V, hold at 4.1 V for 12 h and constant current discharge at 100 mA–0.1 V. The profile of the jelly testing protocol is shown in Figures S3 and S4.

Gas-Decomposed Products Analysis

In-situ Gas chromatography analyses were conducted using a Shimadzu GC-2023 equipped with flame ionization (FID) and thermal conductivity (TCD) detectors. The system features gas phase injection and two distinct columns: one is a SH-Rt™-Msieve 5 Å (50 m length, 0.53 mm inner diameter, 50 µm film thickness, and a temperature range up to 300°C) set at 200°C; the other is a SH-Rt™-Alumina/BOND Na₂SO₄ (50 m length, 0.53 mm inner diameter, 10 µm film thickness, and a temperature range of –10–200°C) set at 180°C for the TCD and FID detectors, respectively. The column temperature was maintained at 40°C. Injection conditions were set to last for 30 seconds, after which the valve was closed, with an argon flow rate of 20 mL/min used as the carrier gas. Helium was used as the makeup gas at flow rates of 8 mL/min and 24 mL/min for the TCD and FID detectors, respectively. Additionally, hydrogen was utilized at a flow rate of 32 mL/min as another carrier gas for the FID detector.

Liquid-Decomposed Product Analysis

The liquid decomposition product was analyzed using two techniques: NMR and GC-MS. NMR spectroscopy was performed using a Bruker Avance III HD 600 MHz system at 25°C. Dimethyl sulfoxide (DMSO-d6) was employed as the solvent and field frequency lock, with 1,4-dinitrobenzene at 1 mg/ml in DMSO-d6 serving as the internal standard. By the way, the GC-MS analysis was carried out with a Perkin Elmer Clarus SQ8T-Clarus680GC system, capable of covering a mass range of 33–350 amu. This system is equipped with an automatic liquid sampler and an Elite-5 ms column (30 m length, 0.25 mm internal diameter, and 0.25 µm film thickness), operating across temperature ranges from –60–325/330°C. The temperature protocol began at 60°C, increased to

180°C at a rate of 25 °C/min, held for 2 minutes, then raised to 280°C and maintained for another 2 minutes. Helium served as the carrier gas at a flow rate of 1.5 mL/min and a split ratio of 150:1. For each analysis, a 1.0 µL sample was injected using a 10 µL syringe. The resulting mass spectra were matched with the NIST/EPA/NIH Mass Spectral Library for compound identification.

Solid-Decomposed Product Analysis

In this study, the composition of materials in the abused electrode and TEABF₄ salt was analyzed using WDXRF on a Bruker S8 Tiger system. To investigate physical morphology and elemental distribution, SEM-EDX were employed using a JEOL JSM-7610F. The chemical structure of the samples was characterized through FTIR on a Perkin Elmer instrument and XPS using a JEOL JPS-9010MC.

Results and Discussion

Physicochemical Characterizations

Table 1 lists a detailed enumeration of the intrinsic characteristics and performance parameters of 18650 supercapacitors, with a particular emphasis on the electrode material composition and overall cell performance. The fabrication of electrodes involves a meticulously balanced slurry comprising AC, Super P, CMC, and SBR in a weight ratio of 92:4:2:2, respectively. This composition is strategically chosen to enhance the electrical conductivity and adhesive properties of the electrodes. The specific BET surface area of the AC is impressively vast at 2302 m²/g, providing a substantial interface for charge accumulation, a critical attribute for supercapacitors. Electrical resistivity

Table 1. Cells and Electrodes Specifications of Our 18650 Supercapacitors.

Electrode properties	Negative electrode: AC	Slurry ratio = AC: Super P: CMC: SBR = 92: 4: 2: 2 Specific surface area of AC powder = 2,302 m ² /g Resistivity = 0.50 Ω/cm ² (± 0.04 Ω/cm ² , n=358) Coating thickness = 211 µm (± 1.36 µm, n=358) Electrode thickness = 199.61 µm (± 3.66 µm, n=358) (Pressing 2 tons) Active mass = 1.33 g (± 0.18 g, n=358)
	Positive electrode: AC	Coating thickness = 211 µm (± 0.05 µm, n=358) Electrode thickness = 199.61 µm (± 3.66 µm, n=358) (Pressing 2 tons) Active mass = 1.33 g (± 0.04 g, n=358)
Cell Capacitances	Cell Weight	26.00 g (± 1.17 g, n = 152)
	Electrolyte	1 M TEABF ₄ in ACN 7.90 g (± 0.20 g, n = 152)
	Separator	Al ₂ O ₃ coated Tri-layer (PP-PE-PP)
Specific capacitances	At 2.7 V	Class 2 110.13 F (± 0.87 F, n = 4) Class 3 108.74 F (± 2.90 F, n = 4)
	At abusive voltage of 2.9 V	Class 4 105.95 F (± 1.05 F, n = 4) Class 2 112.23 F (± 1.20 F, n = 4) Class 3 117.82 F (± 0.43 F, n = 4) Class 4 112.78 F (± 4.42 F, n = 4)
	Volumetric	6.81 F/cm ³
	Gravimetric	4.19 F/g _{cell}
		9.90 F/g _{jelly}
	Internal resistance (IR)	40.98 F/g _{Active materials}
		11.88 mΩ (± 2.15 mΩ, n = 152)

of the electrodes, ascertained at $0.50 \pm 0.04 \Omega \text{cm}$ through the four-point probe method, signifies proficient electrical conduction, a pivotal factor for efficient charge transport. Following a roll-to-roll coating process, the electrode thickness is measured at $211 \pm 1.36 \mu\text{m}$, which is further optimized to $199.61 \pm 3.66 \mu\text{m}$ post-pressing, with the negative electrode exhibiting a mass loading of $1.33 \pm 0.04 \text{ g}$. The cell manufacturing process demonstrates remarkable consistency, as indicated by an average cell weight of $26.00 \pm 1.17 \text{ g}$ across a sample size of 152 cells. The chosen electrolyte, 1 M TEABF₄ in ACN, contributes $7.90 \pm 0.20 \text{ g}$ to the cell weight. Incorporation of an Al₂O₃ ceramic coated tri-layer PP-PE-PP separator is a testament to the design's focus on thermal stability and enhanced electrolyte wettability. Capacitance metrics, gauged across various International Electrotechnical Commission (IEC) Classes at operational voltages of 2.7 V and an elevated 2.9 V, reveal capacitances exceeding 100 F per cell, with both volumetric and gravimetric capacitances being systematically tabulated. Of particular note is the low average internal resistance at 1 kHz, measured at $11.88 \pm 2.15 \text{ m}\Omega$, which plays a crucial role in minimizing energy dissipation during charge-discharge cycles. This low internal resistance is instrumental in facilitating rapid energy exchange processes, thereby minimizing efficiency losses and positioning the supercapacitor as an optimal choice for applications requiring swift energy transitions with minimal performance degradation.

Figure 1 offers a detailed visualization of the microstructural characteristics and assembly processes of 18650 supercapacitors, emphasizing the material properties of the electrodes and the manufacturing stages of the cells. The FESEM image in Figure 1A reveals the irregular shapes of AC particles in the electrodes, a feature that enhances the surface area available for ion adsorption, crucial for the device's storage capacity. The HRTEM image in Figure 1B further exposes the disordered carbon atoms within an AC particle, characteristic of amorphous carbon. This structural disorganization contributes to the material's high electrical conductivity and charge storage capacity, despite lacking crystalline order. Although not visually depicted, the description of three nickel tabs strategically placed in both the negative and positive electrodes (Figure 1C) indicates a design optimized to reduce internal resistance, a critical factor for improving the supercapacitor's efficiency by minimizing energy loss during operation.

The subsequent images transition from microstructural details to assembly processes. Figure 1D shows the jelly-roll cells sans stainless steel casings, submerged in electrolyte within glass test tubes, highlighting a stage possibly related to the manufacturing or testing process. This jelly-roll configuration, with its wound layers of electrodes and separator, aims to maximize the interface between the electrode surface and the electrolyte, thereby boosting the cell's capacitance and energy density. Figure 1E captures a crucial moment during the electrolyte injection process, right before the cell is sealed, ensuring thorough permeation of the electrolyte through the electrode layers for efficient ionic transport. The sequence concludes with Figure 1F, showcasing the final product: blue polyethylene-wrapped cylindrical cells in the 18650-code format

with 18 mm in diameter, 65 mm in height and 0 for a cylindrical configuration, where the wrapping serves both protective and insulating functions, ensuring the cell's safety and stability during use. Together, these images provide a comprehensive view of the electrode material characteristics and the meticulous assembly processes underlying the production of high-performance 18650 supercapacitors.

Figure 2 provides a comprehensive analysis of the electrochemical behavior of 18650 supercapacitors utilizing 1 M TEABF₄ in ACN, under a spectrum of operational conditions. The initial phase of this study, illustrated in Figure 2A and B, delves into the response of these supercapacitors to IEC standard testing at 2.7 V and an elevated voltage of 2.9 V. This exploration underscores the devices' discharge capabilities across distinct classes (2, 3, and 4), each defined by significantly varying current levels, thereby delineating their versatility for diverse power applications. The ability to sustain a high discharge current of 12000 mA in class 4 particularly highlights the supercapacitors' potential for applications necessitating high power output. The rate performance evaluation, encompassed in Figure 2C–D, investigates discharge currents ranging from 100–5000 mA. This segment elucidates variations in capacitance with differing discharge rates (Figure 2C), provides insight into the charge-discharge kinetics via GCD profiles (Figure 2D), and scrutinizes the internal resistance (IR) drop during these tests (Figure 2E), which are pivotal for assessing the supercapacitors' operational efficiency and their capability to withstand varying power demands. The final component of the study, Figure 2F, is dedicated to assessing the durability of the supercapacitors under conditions of prolonged and intensive use. Through constant current charge-discharge testing at 2500 mA (Figure 2F). The cyclic voltammogram of the 18650 cell at 2.5–10 mV/s (Figure 2G) indicates a typical EDLC

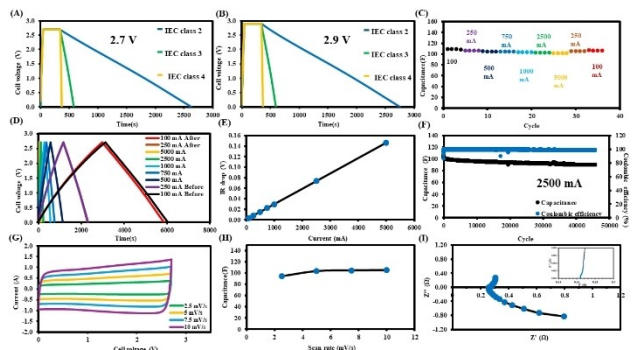


Figure 2. Analysis of Electrochemical Behavior in 18650 Supercapacitors Employing 1 M TEABF₄ in ACN. Panels (A) and (B) depict International Electrotechnical Commission (IEC) standard testing at voltages of 2.7 V and 2.9 V, respectively, across discharge currents corresponding to class 2 (120 mA), class 3 (1200 mA), and class 4 (12000 mA). Panels (C–F) focus on rate performance evaluation across a current range of 100–5000 mA, with (C) showing cell capacitance calculated from GCD, (D) detailing Galvanostatic Charge-Discharge (GCD) profiles, and (E) presenting the instantaneous voltage drop (IR drop) observed during rate performance tests. Panel (F) shows the stability of the cell at 2500 mA. Panels (G–H) show the performance with Cyclic Voltammetry (CV) at 1–10 mV/s, with (G) displaying the Cyclic Voltammogram and (H) showing cell capacitance calculated from CV. (I) shows the Nyquist plot.

behavior, with no gas evolution observed at high potentials. The result here also shows the scan rate independence without diffusion limit in those scan rates indicating high-quality EDLC supercapacitors. The calculated capacitance (Figure 2H) ranges from 94.6–105.0 F. Figure 2I shows the Nyquist plots of the 18650 cell, highlighting key electrochemical processes. Inductive behavior at the negative end is due to the metallic components in the wires and cell. The X-intercept represents the ohmic resistance (R_{e}) from the separator, active material, electrolyte, and current collectors. The semicircle indicates charge transfer resistance (R_{ct}) at the electrolyte/electrode interface and double-layer capacitance. At lower frequencies, diffusion processes within the active materials are observed, which is in good agreement with previous report,^[8] the investigation appraises the supercapacitor endurance in sustaining performance levels under considerable power loads. Altogether, this multi-faceted analysis presents an extensive overview of the electrochemical attributes of the 18650 supercapacitors, evidencing their resilience, operational efficiency, and adaptability to a broad array of electrical loads and conditions. This informs their suitability for a diverse range of technological applications.

Electrochemical Test

Figure 3 offers a detailed performance analysis of AC electrode-based 18650 cylindrical cell EDLCs, employing 1 M TEABF₄ in ACN as the electrolyte, with water content levels ranging from 0–1600 ppm. This rigorous examination assesses the impact of water content on the electrochemical performance of supercapacitors through GCD cycles at various current densities, specifically at 2.7 V. Observations from Figure 3A and B reveal that coulombic efficiency remains nearly flawless across all current densities examined, with GCD curves at initial and

subsequent cycles at 250 mA and 500 mA displaying significant consistency. This finding attests to the electrodes' resilient performance, validating their potential for extensive experimental applications. Further exploration into the effect of water content on EDLC performance is detailed in Figure 3C and D, focusing on the relationship between water content and both coulombic and energy efficiencies at 2.7 V. The data delineate a progressive decline in supercapacitor performance with increasing water content, indicating a complex interplay between water molecules, the electrolyte's ionic conductivity, and electrode surface characteristics. To elucidate potential degradation mechanisms within these EDLCs associated with varying water content, additional investigations were undertaken under enhanced stress conditions (4.1 V), including prolonged durations at open circuit voltage (OCV) and abusive voltages for 12 h, followed by a discharge to 0.1 V using a constant current of 100 mA. The degradation trajectory is meticulously mapped through further GCD profiles and rate capability assessments at current densities of 100 mA and 250 mA, and notably, following exposure to a rigorous 2500 mA. These assessments disclose a noticeable deviation in GCD curves, albeit within the predefined thresholds (grey and blue dotted lines), indicating the commencement of supercapacitor degradation. Figure S5 shows the CV and EIS results, where the CV study in the voltage range of 2.4–2.7 V indicates gas evolution. The increased water content in the electrolyte solution leads to a higher level of gas evolution (Figure S5a–b). The analytical scope was broadened to include post-experimentation examination of the electrolyte's decomposition products via GC-MS and NMR for liquid phase analysis, which encompassed water, ACN, and acetamide derivatives. The solid phase was subjected to SEM-EDX, WDXRF, FTIR, and XPS to unveil material alterations. Moreover, gas evolution was monitored employing DEMS and in-situ GC-FID/TCD techniques. This integrative methodological approach not only illuminates the operational stability and degradation pathways of the EDLCs under assorted water content and stress conditions but also highlights the critical role of exhaustive material characterization in deciphering supercapacitor performance and longevity.

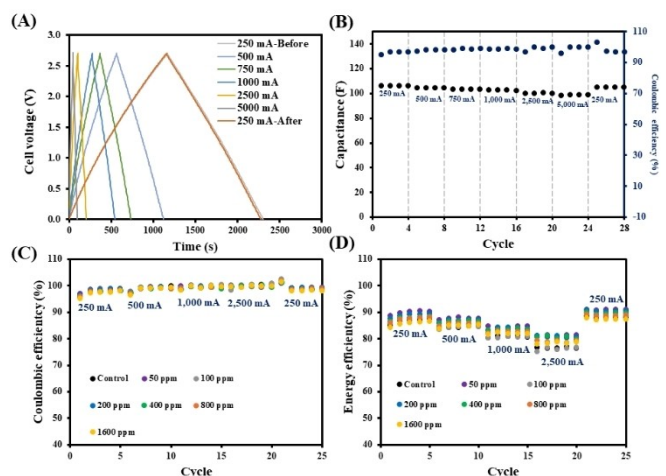


Figure 3. Performance Evaluation of Activated Carbon Electrode 18650 Jelly Roll Utilizing 1 M TEABF₄ in ACN; Panel (A) depicts GCD curves at various current densities, while Panel (B) illustrates the rate capability assessed at differing current densities. Panels (C) and (D) analyze the impact of water content on the coulombic efficiency and energy efficiency, respectively, at an operational voltage of 2.7 V.

Electrolyte Decomposition in Gas-Phase Byproducts

The analysis of gas decomposition products from 18650 EDLCs, as explored in Figure 4A and detailed in Table 2, offers insightful observations into the electrochemical stability and degradation mechanisms of these supercapacitors under abusive voltage conditions (4.1 V) with varying water content. The in-situ GC-FID/TCD results identify ethylene, ethane, and nitrogen as the primary decomposition products, with carbon dioxide, carbon monoxide, and hydrogen being the minor ones. The data underscores a correlation between the increasing water content in the electrolyte and the quantity of gas decomposition products, indicating that water exacerbates the degradation process. Ethylene formation, a significant decomposition outcome, arises through the Hofmann elimination reaction of TEABF₄.^[9] This reaction mechanism involves the

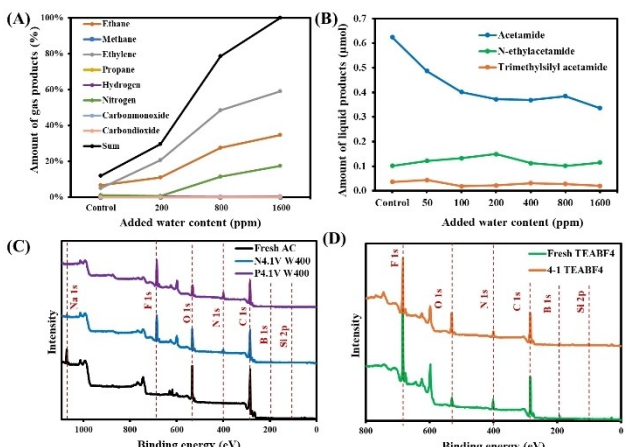


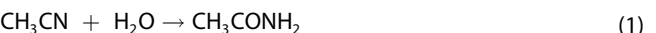
Figure 4. Analysis of Decomposition Products and XPS Wide Scan Spectra Under Abusive Conditions; Panel (A) illustrates the gas-phase decomposition via GC-FID/TCD and Panel (B) the liquid-phase decomposition at 4.1 V across different water concentrations via NMR. Panels (C) and (D) present X-ray Photoelectron Spectroscopy (XPS) wide scan spectra for the activated carbon (AC) electrode and tetraethylammonium tetrafluoroborate (TEABF_4) salt, respectively, at 4.1 V with 400 ppm water, highlighting changes in the surface chemistry and elemental composition.

transformation of quaternary amines into tertiary amines and alkenes, coupled with the elimination of a proton. The process is sensitive to temperature and voltage, with both factors accelerating the rate of ethylene formation. Notably, the presence of water further catalyzes this reaction, hinting at the intricate role of water in facilitating electrolyte decomposition under thermal and electrical stress. Ethylene, alongside triethylamine, emerges as a notable degradation by-product, particularly affecting the negative electrode during its aging process.

The examination of gas-phase decomposition products emanating from 18650-cylindrical EDLC cells, as delineated in Figure 4A and elucidated in Table 2, furnishes valuable insights into the electrochemical resilience and deterioration pathways of these supercapacitors when subjected to abusive voltage conditions (4.1 V) alongside variable water concentrations. The employment of in-situ GC-FID/TCD methodology facilitates the identification of ethylene, ethane, and nitrogen as predominant decomposition byproducts, with carbon dioxide, carbon monoxide, and hydrogen categorized as secondary emissions. The empirical evidence highlights a direct association between augmented water content within the electrolyte and an escalation in the volume of gas-phase decomposition products, signifying that water acts as a catalyst in the degradation

mechanism. The genesis of ethylene, a principal decomposition by-product, is attributed to the Hofmann elimination reaction pertinent to TEABF_4 . This reaction pathway encompasses the conversion of quaternary amines to tertiary amines and alkenes, concomitant with the expulsion of a proton. Both temperature and voltage emerge as critical factors expediting the formation of ethylene, wherein the involvement of water further enhances this reaction, underscoring the complex interplay of water in promoting electrolyte decomposition under conditions of thermal and electrical duress. The emergence of ethylene, alongside triethylamine, as a significant degradation by-product, notably impinges on the aging trajectory of the negative electrode, shedding light on the nuanced mechanisms of electrode deterioration.

The other gas decomposition products were ethane and nitrogen. Regarding the reaction mechanisms, the hydrolysis of ACN (CH_3CN) can form acetamide (CH_3CONH_2), as shown in reaction (1).^[5b,9] Further hydrolysis of acetamide leads to the formation of acetic acid^[9] and ammonia, as indicated in reaction (2). Additionally, ammonia is produced through the degradation of acetamide in the presence of functional groups like $-\text{OH}$ or $-\text{COOH}$, which are typically found on the surface of activated carbon electrodes (reactions 3 and 4).



Besides, the formation of nitrogen gas (N_2) in ACN-based supercapacitor systems at elevated voltages or temperatures has been previously attributed to the direct oxidation of ammonia (NH_3), as reported by Sun et al.^[10]

In our system, containing 1600 ppm of water, additional reactions (5–7) proceed via the well-established electrooxidation mechanisms of NH_3 in a high-pH basic solution (pH 9–10) resulting from water decomposition. These reactions yield N_2 , NO_2^- , and NO_3^- as products, respectively.^[11]

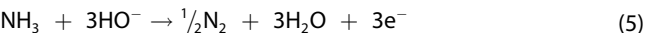


Table 2. Variation in gas decomposition product quantities under an abusive voltage of 4.1 V across different water contents.

Water content	Methane (CH_4)	Ethane (C_2H_6)	Ethylene (C_2H_4)	Propane (C_3H_8)	Hydrogen (H_2)	Nitrogen (N_2)	Carbon monoxide (CO)	Carbon-dioxide (CO_2)
Control	0.02 %	6.80 %	5.04 %	0.01 %	0.00 %	1.35 %	0.05 %	0.16 %
200 ppm	0.01 %	11.08 %	20.74 %	0.01 %	0.64 %	0.72 %	0.02 %	0.12 %
800 ppm	0.05 %	27.70 %	48.58 %	0.02 %	0.27 %	11.48 %	0.03 %	0.12 %
1600 ppm	0.04 %	34.80 %	59.10 %	0.03 %	0.46 %	17.62 %	0.06 %	0.25 %

The in-situ GC-FID/TCD analysis presented in Table 2 confirms the production of N_2 gas, as indicated in reaction (5). Additionally, the presence of NO_2^- and NO_3^- was verified through UV-Vis spectroscopy (see Figure S6).^[12] In addition, this research found a small amount of methane, propane, hydrogen, carbon dioxide, and carbon monoxide as listed in Table 2, which are in good agreement with other reports.^[5b,9–10]

Electrolyte Decomposition in Liquid-Phase Byproducts

In this study, we have conducted an in-depth analysis of the hydrolysis of ACN into acetamide,^[9] as demonstrated using NMR and GC-MS techniques shown in Figure S7. Which subsequently undergoes further decomposition to yield N-ethyl acetamide and trimethylsilyl acetamide. This decomposition sequence is facilitated by catalytic actions of chemical groups and trace silicon elements inherent to the electrode surface, as depicted in Figure 5. Our research is particularly concentrated on assessing the influence of water content on the formation of three principal liquid decomposition by-products. The investigative process entailed monitoring the liquid decomposition under an abusive voltage condition of 4.1 V across varying levels of water content over a duration of 12 h. Utilizing NMR spectroscopy, we identified the three main electrolyte degradation products: acetamide, N-ethyl acetamide, and trimethylsilyl acetamide. It was observed that the presence of water markedly impacts the concentration of acetamide; specifically, elevating the water content to 1600 ppm resulted in a decrease in acetamide concentration from 0.62 μmol –0.34 μmol , as delineated in Table 2 and illustrated in Figure 4b. This diminution in acetamide levels coincided with the detection of additional degradation by-products, including diisopropylamine, N, N-diethyl urea, and N, N-diethyl acetamide, as determined through GC/MS analysis. Concerning the concentrations of N-ethyl acetamide and trimethylsilyl acetamide, our results did not exhibit a consistent pattern in relation to variations in water content, suggesting that their formation is not directly modulated by water concentrations. Instead, the synthesis of these compounds seems to be influenced by the electrode's chemical functionalities and the presence of contaminants, such as

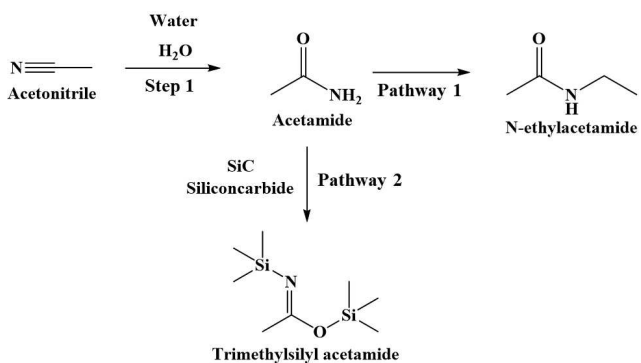


Figure 5. The proposed reaction mechanisms of electrolytes leading to liquid-phase byproducts.

silicon, within the cell structure. The reaction mechanism involves acetonitrile and water, leading to the formation of acetamide, N-ethyl acetamide, and trimethylsilyl acetamide, highlighting the complex interplay between water content and electrode surface chemistry in the degradation process.

Post-Mortem Analyses of Solid Electrodes

Figure 6 and associated analyses delve into the degradation mechanisms of electrodes in supercapacitors, focusing on changes in the functional groups and elemental composition of fresh versus abused electrodes. This investigation utilizes a suite of analytical techniques, including XRF, SEM-EDX, FTIR and XPS, to elucidate the effects of abusive voltage conditions (4.1 V) with varied water content on electrode materials. The results of the analysis using the WD-XRF technique are shown in Table S3. The activated carbon material obtained, which is produced from biomass, was found to contain Si at a concentration of 0.088% and aluminum (Al) at 0.007%. When subjected to abusive voltage conditions with different water contents, a notable shift in elemental composition is observed: the silicon content decreases while the aluminum content increases. This trend is attributed to the use of aluminum foil as the current collector in the supercapacitors, which undergoes specific aging mechanisms under the given experimental conditions. The aging mechanisms for the current collectors are categorized into corrosion and anodic dissolution. Corrosion is described as a spontaneous reaction between the current collector and surrounding compounds, dependent on their reactivity and the products they form. Anodic dissolution, on the other hand, necessitates an electrical current to oxidize the current collector. These processes highlight the complex interactions between the electrode materials and the operational environment, particularly under conditions that simulate abuse (high voltage and water content). Such degradation mechanisms have profound implications for the durability and performance of

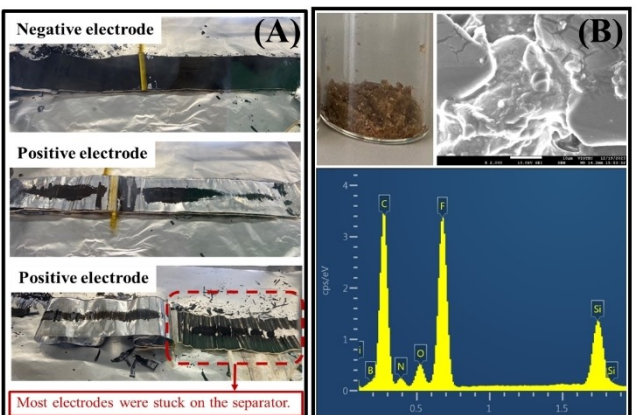


Figure 6. Panel (A) depicts electrodes of activated carbon (AC) subjected to stress testing, illustrating the morphological changes due to abusive conditions. Panel (B) showcases SEM-EDX analysis of $TEABF_4$ salt after exposure to a 4.1 V abusive voltage condition with an addition of 400 ppm water, revealing the alterations in elemental composition and surface morphology.

supercapacitors. The increase in aluminum content could be indicative of the corrosion or dissolution of the aluminum foil current collector,^[13] potentially compromising the supercapacitor's structural integrity and electrical conductivity over time. Conversely, the decrease in silicon content suggests a loss or transformation of silicon-based compounds or contaminants within the electrode material, which could alter the electrode's surface properties and, consequently, its electrochemical performance. In summary, Figure 6, along with the detailed analytical results, provides valuable insights into the degradation pathways of supercapacitor electrodes under abusive conditions. Understanding these mechanisms is crucial for improving the design and material selection in supercapacitors, aiming to enhance their resilience and longevity in various applications.

The XPS wide spectra of the AC electrode, as shown in Figure 4C, particularly at 4.1 V with 400 ppm of added water in the electrolyte, highlight the presence of elements such as C, F, N, Na, B, Si, and O, which are identified in the solid decomposition in supercapacitors. A comparison of elements in fresh, abused positive, and abused negative electrodes (Table S2) reveals that N, F, and B are present in both abused electrodes. WDXRF result in Table S3 also confirmed this XPS result. However, Na is absent in the abused positive electrode. Si traces are found in the fresh electrode and both sides of the abused electrode, though in lesser quantities than in the fresh electrode. This indicates that Si in the AC electrode is reduced after SC use, possibly transforming into other products in the electrolyte, such as trimethylsilyl acetamide found in the liquid decomposition. Additionally, the presence of the Si element is detected in the abused TEABF₄ salt at 4.1 V with 400 ppm of added water.

Figure 7 offers a comparative analysis of the FTIR spectra for fresh versus abused electrodes under varying water content conditions, focusing on both positive and negative electrodes. Figure 7A and B display the FTIR spectra of negative and positive electrodes, respectively. The fresh electrode's FTIR spectrum appears smooth, indicating minimal functional group diversity or degradation products. In contrast, the spectra of abused electrodes reveal a more complex composition, high-

lighting the impact of operational stress on the electrode material. For both the positive and negative electrodes of the abused samples, common functional groups such as carbonyl (O=C=O and C=O), cyanide (C≡N), and ether (C—O) were identified, suggesting similar pathways of degradation or contamination across both electrode types. The distinction in functional groups between the positive and negative electrodes becomes apparent with the observation of C—F (carbon-fluorine) and O—H (hydroxyl) stretching at 570 cm⁻¹ and 1400 cm⁻¹, respectively, on the positive electrode. This implies the presence of fluorinated compounds and possibly water absorption or hydroxyl group formation on the electrode surface, indicative of electrolyte decomposition and interaction with the electrode material. On the negative electrode, aromatic C—C and C—N stretching vibrations were detected at 780 cm⁻¹ and 1455 cm⁻¹, respectively. These functional groups suggest the presence of aromatic structures and cyano groups, which could be attributed to the degradation of the electrolyte, or the modification of the carbon material used in the electrode.

The primary functional groups identified—C—F stretching on the positive electrode and C—N stretching on the negative electrode—reflect the composition of the TEABF₄ electrolyte and its interaction with the electrode material. The presence of these functional groups signifies the complete supercapacitor system's response to the abusive conditions tested. This analysis underscores the chemical changes and degradation mechanisms that occur in supercapacitor electrodes under stress conditions, providing insights into the stability and longevity of these devices in real-world applications. Understanding these changes is crucial for the design and development of more durable and reliable supercapacitors.

Conclusions

This study presents a comprehensive investigation into the effects of water impurities on the decomposition of ACN-based electrolytes in large-scale cylindrical supercapacitors. Utilizing advanced analytical techniques, the research identified the formation of significant gaseous byproducts such as ethylene, ethane, and nitrogen, alongside liquid-phase products including acetamide, N-ethyl acetamide, and trimethylsilyl acetamide. These findings underscore the critical role of water impurities in accelerating electrolyte degradation, elucidating the complex pathways involved in this process, notably through Hofmann elimination and hydrolysis reactions. The presence of water was found to catalyze the formation of new byproducts, impacting the stability and performance of both electrolytes and electrodes. In-situ gas chromatography and nuclear magnetic resonance provided detailed insights into the kinetics and mechanisms of these decomposition reactions, revealing that even trace amounts of water can significantly influence the degradation behavior of supercapacitors. The study's outcomes demonstrate that controlling water content is paramount to mitigating decomposition processes, thereby enhancing the longevity and efficiency of supercapacitors. The implications of these findings are profound for the design and development of supercapaci-

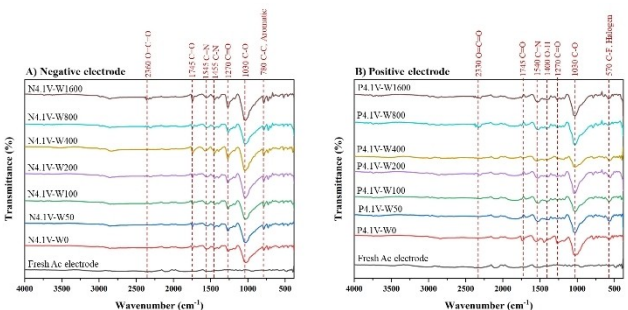


Figure 7. FTIR Spectra Analysis of Electrodes Subjected to Abusive Voltage Conditions at 4.1 V Across Different Water Concentrations; Panel (A) displays the spectrum for the negative electrode, and Panel (B) illustrates the spectrum for the positive electrode, showcasing the alterations in the chemical bonds and functional groups as a consequence of the varying water content.

tors. By highlighting the detrimental effects of water impurities, this research paves the way for the formulation of strategies to minimize these effects. Potential approaches include the development of more robust electrolyte compositions with enhanced stability and lower water susceptibility, as well as the optimization of electrode materials to better withstand the presence of impurities. Additionally, stringent purification protocols should be implemented to reduce water contamination during the manufacturing process.

Acknowledgements

This work was financially supported under Program Management Unit for National Competitiveness Enhancement (PMU-C) by Office of National Higher Education Science Research and Innovation Policy Council (NXPO) and IRPC Public Company Limited, Thailand Science Research and Innovation (TSRI) under the Fundamental Fund by TSRI (FRB680014/0457) and Vidyasirimedhi Institute of Science and Technology (VISTEC) as well as Energy Policy and Planning Office (EPPO), Ministry of Energy, Thailand. In addition, the Frontier Research Centre (FRC) supported this work, VISTEC.

Conflict of Interests

There is no conflict of interest.

Data Availability Statement

The data that support the findings of this study are available from the corresponding author upon reasonable request.

Keywords: Energy storage • Supercapacitors • Electrolyte decomposition • Reaction mechanisms

- [1] A. Burke, *J. Power Sources* **2000**, *91*, 37–50.
- [2] a) P. Simon, Y. Gogotsi, *Nat. Mater.* **2008**, *7*, 845–854; b) P. Simon, Y. Gogotsi, B. Dunn, *Science* **2014**, *343*, 1210–1211; c) J. Zhao, A. F. Burke,

Adv. Energy Mater. **2021**, *11*, 2002192; d) J. Zhao, A. F. Burke, *Energy Storage Mater.* **2021**, *36*, 31–55.

- [3] a) A. Mohamed, E. M. Wazeer, S. M. El Masry, A. M. A. Ghany, M. A. Mosa, *J. Energy Storage* **2024**, *89*, 111799; b) A. P. Wibisono, A. Muhamar, A. C. Budiman, A. Hapid, K. Ismail, R. Ristiana, S. Kaleg, M. A. P. Perdana, *Evergreen* **2023**, *10*, 1862–1867; c) Q. Zhang, K. Wei, *Int. J. Electrochem. Sci.* **2024**, *19*; d) G. Shini, J. L. Febin Daya, P. Balamurugan, *J. Appl. Res. Technol.* **2024**, *22*, 42–51.
- [4] a) A. Burke, *Int. J. Energy Res.* **2010**, *34*, 133–151; b) A. F. Burke, J. Zhao, *Appl. Sci. (Switzerland)* **2022**, *12*, 1726; c) A. F. Burke, J. Zhao, *J. Energy Storage* **2021**, *35*, 102310.
- [5] a) E. Pameté, L. Köps, F. A. Kreth, S. Pohlmann, A. Varzi, T. Brousse, A. Balducci, V. Presser, *Adv. Energy Mater.* **2023**, *13*, 2301008.; b) P. Kurzweil, M. Chwistek, *J. Power Sources* **2008**, *176*, 555–567; c) H. Park, H. Yong, J. Jung, C. Jung, *ChemElectroChem* **2019**, *6*, 4418–4428; d) P. Wuamprakhon, J. Phojaroen, T. Sangsanit, K. Santiyuk, K. Homlamai, W. Tejangkura, M. Sawangphruk, *ChemSusChem* **2024**, *17*, e202400053; e) L. Köps, F. A. Kreth, M. Klein, A. Balducci, *J. Power Sources* **2023**, *581*, 233480.
- [6] a) R. Songthan, T. Sangsanit, K. Santiyuk, K. Homlamai, W. Tejangkura, M. Sawangphruk, *J. Electrochem. Soc.* **2024**, *171*, 050524; b) T. Sangsanit, K. Santiyuk, R. Songthana, K. Homlamai, S. Prempluem, W. Tejangkura, M. Sawangphruk, *J. Power Sources* **2024**, *611*, 234770; c) T. Sangsanit, K. Homlamai, N. Joraleechanchai, S. Prempluem, W. Tejangkura, M. Sawangphruk, *J. Power Sources* **2024**, *594*, 234021; d) S. Prempluem, T. Sangsanit, K. Santiyuk, K. Homlamai, W. Tejangkura, R. Songthan, N. Anansuksawat, M. Sawangphruk, *J. Power Sources* **2024**, *606*, 234538; e) N. Anansuksawat, T. Sangsanit, S. Prempluem, K. Homlamai, W. Tejangkura, M. Sawangphruk, *Chem. Sci.* **2024**, *15*, 2026–2036.
- [7] a) S. Kaenket, P. Suktha, K. Kong sawatvoragul, T. Sangsanit, P. Wuamprakhon, R. Songthan, W. Tejangkura, K. Santiyuk, K. Homlamai, M. Sawangphruk, *J. Power Sources* **2023**, *581*, 233512; b) S. Zhou, *J. Phys. Chem. C* **2019**, *123*, 29638–29646; c) J. R. Yoon, E. Baek, H. K. Kim, M. Pecht, S. H. Lee, *Carbon* **2016**, *101*, 9–15.
- [8] P. Wuamprakhon, R. Donthongkwa, K. Hantanasirisakul, V. Promarak, J. Limtrakul, M. Sawangphruk, *Chem. Commun.* **2021**, *57*, 13712–13715.
- [9] a) F. A. Kreth, L. H. Hess, A. Balducci, *Energy Storage Mater.* **2023**, *56*, 192–204; b) J. M. Lim, Y. S. Jang, H. V. T. Nguyen, J. S. Kim, Y. Yoon, B. J. Park, D. H. Seo, K.-K. Lee, Z. Han, K. K. Ostrikov, *Nano. Adv.* **2023**, *5*, 615–626;
- [10] Q. Sun, Z. Yi, Y. Fan, L. Xie, Z. Wang, G. Sun, Z. Wang, X. Huang, Z. Liu, F. Su, C. Chen, *ACS Appl. Mater. Interfaces* **2023**, *15*, 54386–54396.
- [11] N. J. Bunce, D. Bejan, *Electrochim. Acta* **2011**, *56*, 8085–8093.
- [12] Q.-H. Wang, L.-J. Yu, Y. Liu, L. Lin, R.-G. Lu, J.-P. Zhu, L. He, Z.-L. Lu, *Talanta* **2017**, *165*, 709–720.
- [13] E. Krämer, T. Schedlbauer, B. Hoffmann, L. Terborg, S. Nowak, H. J. Gores, S. Passerini, M. Winter, *J. Electrochem. Soc.* **2013**, *160*, A356.

Manuscript received: November 18, 2024

Accepted manuscript online: November 20, 2024

Version of record online: December 10, 2024